IMPROVED ANALYSIS OF SPREADING RESISTANCE MEASUREMENTS

Scott T. Dunham, Nat Collins[1] and Nanseng Jeng[2]
Department of Electrical, Computer and Systems Engineering
Boston University, Boston, MA

In this paper, we describe a system for the analysis of spreading resistance data which includes carrier spilling through the solution of Poisson's equation. The Poisson equation solution requires boundary conditions for the charge density on the beveled surface, which we model by considering the presence of surface states with levels within the band-gap. Considering surface states allows the deviation from ideality of both n- and p-type calibration curves to be accounted for consistently without empirical contact resistance or variable radius corrections. In addition, we consider the effects of finite probe penetration and change in energy gap due to probe pressure to account for the reduction in peak resistance near junctions observed experimentally as compared to theoretical calculations. The software (SERAPES) can be used both to calculate simulated resistance profiles from doping profiles for process model characterization as well as to calculate doping profiles directly from spreading resistance measurements.

1 Introduction

Spreading resistance profiling is a widely-used method for determining dopant profiles in semiconductors [1, 2]. The demand for increased accuracy in this technique, driven by the reduction in junction depths in integrated circuit devices, requires more sophisticated spreading resistance analysis. Standard analysis techniques assume charge neutrality throughout the sample, which implies that carrier concentrations and resistivity depend only on the local doping concentration. However, in non-uniformly doped material, carriers diffuse from more heavily-doped regions to areas of lower carrier concentration, limited by the resulting electric field. This effect is commonly referred to as "carrier spilling" [1, 3, 4, 5]. The effects of carrier spilling on spreading resistance are particularly strong in regions of large doping gradients and near junctions and result in inaccurate determination of doping profiles and junction depths when these effects are not considered. To correctly calculate the distribution of carriers, and thus the dependence of resistivity on position which determines the measured spreading resistance, it is necessary to solve Poisson's equation.

In this paper, we describe a system (SERAPES) for the improved analysis of spreading resistance data. We begin by describing a framework for the analysis of spreading resistance, including the effects of carrier spilling, in Section 2. In Section 3, we discuss the effect of surface charges on spreading resistance measurements and compare the results of surface state models to calibration data. In Section 4, we discuss the effect of probe penetration and pressure on spreading resistance profiles and introduce methods to consider these effects in the calculations. Section 5 describes our spreading resistance analysis system and an

[1]Current address: Texas Instruments, Houston TX
[2]Current address: Research and Development, Micron Semiconductor, Boise ID

example of its application. Finally, Section 6 summarizes our conclusions.

2 Spreading Resistance Analysis Including Carrier Spilling

The goal of spreading resistance measurements is to determine the doping profile in a sample as a function of depth ($N(x)$) based on a series of two-probe resistance measurements. However, this is an inverse problem, which can only be solved by iterating on solutions to the direct problem: calculation of the resistance which would be measured for a given doping profile. Therefore, we will begin by considering the direct problem, calculating resistance from doping.

A one-dimensional doping profile can be approximated by a multilayer structure, that is a set of $m-1$ thin layers (thickness Δx), each with constant doping N_i, on top of a semi-infinite substrate with doping N_m. The structure is illustrated in Figure 1. Spreading resistance analysis assumes that between each measurement, a thin layer is removed from the surface. Typically, the measurements are actually made by stepping a distance Δl along a beveled sample, but as long as the bevel angle is small, two-dimensional effects are negligible [3] and $\Delta x = \Delta l \sin\theta$. Thus, each resistance measurement R_i ($i = 1, \ldots, m$) is effectively made on a structure consisting of layers N_i to N_m (equivalent to etching off the top layers, 1 to $i-1$).

Standard techniques further assume charge neutrality, so that the carrier concentrations can be calculated directly from the local doping density. However, the carrier concentrations actually depend on the solution of Poisson's equation, which in one-dimension (appropriate for an unpatterned sample) is

$$\frac{d^2\psi(x)}{dx^2} = -\frac{q}{\epsilon}\left[N(x) + p(\psi) - n(\psi)\right], \tag{1}$$

where ψ is the local potential, q is electronic charge, ϵ is the dielectric constant, $N(x) = N_D^+(x) - N_A^-(x)$ is the net doping, and p and n are the hole and electron concentrations. The carrier concentrations are assumed to be near equilibrium, since the applied voltages are very small ($\sim$ 5mV) and changes in the minority carrier concentration due to injection would have a negligible effect on the resistivity. Thus, we can define ψ as the difference between the Fermi level and the intrinsic Fermi level ($\psi = (E_f - E_i)/q$) so that

$$n(\psi) = n_i \exp\left[\frac{q\psi(x)}{kT}\right] \quad \text{and} \quad p(\psi) = n_i \exp\left[\frac{-q\psi(x)}{kT}\right] = \frac{{n_i}^2}{n(\psi)}, \tag{2}$$

where T is temperature, k is Boltzmann's constant and n_i is the intrinsic carrier concentration.

Deep in a uniformly-doped substrate, the electric field approaches zero so that,

$$\left.\frac{d\psi}{dx}\right|_{\infty} = 0. \tag{3}$$

Since by beveling we have effectively removed the top portion of the profile, in calculating R_i the top surface is located at $x_i = (i-1)\Delta x$. At the surface, the electric field is proportional to the surface charge,

$$\left.\frac{d\psi}{dx}\right|_{x_i} = -\frac{Q_{ss}}{\epsilon}. \tag{4}$$

In previous analysis of carrier spilling, it has usually been assumed that the surface charge is zero or a constant independent of surface potential [1, 2, 4, 6, 7]. However, as we discuss further in Section 3, the surface would be expected to be characterized by a density of surface-states so that $Q_{ss} = f\left[\psi(x_i)\right]$.

The carrier concentration profiles from the Poisson equation solution and the doping profile can be used to calculate the conductivity profile,

$$\sigma_i = q\left[\mu_n(N_i)n(x_i) + \mu_p(N_i)p(x_i)\right], \tag{5}$$

with the mobilities determined from look-up tables or parametric equations fit to experimental data. Given the conductivity or resistivity as a function of depth, the resistance which would be measured is given by

$$R = \frac{\mathcal{C}}{2\sigma(0)a} = \frac{\mathcal{C}\rho(0)}{2a}, \tag{6}$$

where a is the probe radius and $\mathcal{C}$ is a correction factor accounting for the non-uniform doping. As first analyzed by Schumann and Gardner [8], $\mathcal{C}$ can be approximated by an integral. Since there is a choice in the approximations made in reducing the three-dimensional system to one dimension, there are several possible formulations [1], but the differences between the results of the different approximations are small [9]. Therefore, we use the EMAP algorithm proposed by Berkowitz and Lux [10], which is very efficient and has been shown to give good results. The correction factor for the measurement of R_i in the EMAP algorithm is given by

$$\mathcal{C}_i = \frac{8}{\pi}\int_L^\infty F_i(\lambda)\left[\frac{J_1(\lambda a)}{\lambda a}\right]^2 d\lambda, \tag{7}$$

where λ is a dummy integration variable, $L = 1.12292/S$ (S is the probe separation), J_1 is the Bessel function, and F_i contains all the information about the conductivity profile. Returning to the multi-layer model, F_i can be expressed in terms of a recursion relation [11]:

$$F_i = \frac{F_{i+1}\sigma_i + \sigma_{i+1}\tanh(\lambda\Delta x/a)}{\sigma_{i+1} + F_{i+1}\sigma_i\tanh(\lambda\Delta x/a)}, \tag{8}$$

with $F_m = 1.0$. This recursion relation can be generalized for varying layer thicknesses by replacing Δx with $\Delta x_i = x_{i+1} - x_i$, the thickness of layer i. We use the more general form so that we can use a nonuniform grid for the Poisson solution and reduce computation time. In the standard analysis, use of the recursion relation is very efficient since the correction factor at each level can be calculated easily from the previous value. However, when carrier spilling is considered, Poisson's equation must be solved again each time a layer is added or removed, and thus the conductivity profile changes so that the results of previous calculations cannot be used in the recursion relation.

To reconstruct doping from measured resistance requires finding the doping profile which would result in the measured resistance values. There are three basic techniques which can be used. First, the problem can be considered an m-dimensional optimization problem in which the doping in each layer and the substrate is allowed to vary to best match the measurements. Since m values are varied to match m measurements, it is possible to match the data exactly. However, due to noise in the measured data, the resulting profiles are extremely irregular and producing physically reasonable profiles requires adding a smoothness criterion [12]. An additional barrier to using this approach is that it is extremely expensive computationally [13], particularly with numerical derivatives requiring m Poisson solutions at each iteration, and the computation is prohibitive for many applications. The second alternative is to use a parametric description of the doping profile. This technique is very useful for comparing measurements to model predictions, such as the output of process simulators [14, 15]. This technique is used in SRP2 [7], where either a process simulator or a parameterized analytic function can be optimized. Measurement noise is not a problem since only smooth trial functions are used. The main pitfall with these techniques are that solutions are limited by the choice of trial functions and can result in self-fulfilling predictions if great care is not taken. The third technique for inversion arises from noting that each resistance measurement depends only on the underlying layers. Thus, it is possible to build up the doping profile starting with the substrate and moving towards the surface [16]. For each measured value, a layer is added to the profile. The doping in the top layer is chosen such that the calculated and measured resistances match, while the doping in the underlying layers remains fixed. Thus, the measured data can be matched exactly, just as in the full optimization (without smoothing or a smoothness constraint, the results are the same). However, noise is a major problem and the data must first be smoothed in order to get reasonable results. In this work, we use both the second and third techniques as described further in Section 5.

3 Surface State Model and Calibration Techniques

In order to quantify spreading resistance measurements, calibration samples with constant doping and known resistivity are used. If surface charges are neglected, the carrier concentrations are also constant, even using a Poisson solution. Thus, F is unity and the correction factor can be calculated from Equation (7) to be $\mathcal{C}_0 = 1.081 - 0.715S/a$, independent of doping level, and thus $R = (\mathcal{C}_0\rho/2a)$. However, when calibration samples are actually measured, the slope of the resulting $\log R$ versus $\log \rho$ calibration curves significantly deviate from unity. Previous work has accounted for this discrepancy by adding a barrier resistance ($R_i = \mathcal{C}_i\rho_i/2a + R_{\text{barrier}}$) [6, 17, 18], or allowing the probe contact radius to vary with surface resistivity ($a = a(\rho_i)$) [12, 19, 20]; however, these corrections are strictly empirical and may not remain valid on nonuniformly-doped samples.

In order to account for these effects in a more fundamental physical manner, we note that semiconductor surfaces are typically characterized by a density of surface states resulting from dangling bonds and damage near the surface. The simplest model for surface charge would be to assume that the ionization energies of the surface states are outside the band gap and thus the surface has a fixed areal charge density Q_{ss}. This approach has been used previously to account for some anomalies in spreading resistance profiles [3, 6]. At the opposite extreme, it may be assumed that the metal-work function difference or a very high density of surface states effectively pins the location of the Fermi level [21]. More generally, we can assume that the density of surface states is a function of position in the gap. However, since the calibration data is limited, it is necessary to assume that the surface state density can be described by a limited number of parameters. In this work, we have considered fixed charge, a uniform surface state density and discrete levels, as well as combinations of these distributions.

In general, the surface charge due surface states can be written

$$\begin{aligned}Q_{ss} = Q_{ss}^{+} - Q_{ss}^{-} &= q\int_{-\infty}^{\infty} N_D'(E)\left[1 - f(E - q\psi_s)\right] - N_A'(E) f(E - q\psi_s)\, dE \\ &= q\int_{-\infty}^{\infty} N_D'(E) - q\int_{-\infty}^{\infty} \left[N_D'(E) + N_A'(E)\right] f(E - q\psi_s)\, dE, \end{aligned} \tag{9}$$

where $f(E - q\psi_s)$ is the probability of electron occupation and $N_D'(E)$ and $N_A'(E)$ are the densities of donor and acceptor states per unit energy. The surface potential $q\psi_s$ is measured relative to the intrinsic Fermi level E_i. We have assumed that the spacing between the donor and acceptor energy level for any one defect is much greater kT so that we do not have to subtract the number of surface donors when calculating the number of surface acceptors and vice-versa. Because $f(E)$ drops monotonically from $f(-\infty) = 1$ to $f(\infty) = 0$, for a uniform density of surface states ($N_D(E) + N_A(E) = N_{ss}'$), Equation (9) reduces to

$$Q_{ss} = Q_{ss}^{0} + q^2 N_{ss}' \psi_s, \tag{10}$$

where Q_{ss}^{0} is the surface charge density when the surface potential is equal to the intrinsic Fermi level ($\psi_s = 0$).

When we compare different interface models to our calibration data, we find that even simple models of the surface state density do an excellent job of matching experimental calibration data. This may be due to the fact that surface states have the greatest effect on substrate conductivity for lightly-doped material, so the interface state density near midgap is of primary importance. Figure 2 shows a comparison of ideal behavior ($R = \mathcal{C}_0\rho/2a$), a barrier resistance model and the uniform state density model to both n- and p-type calibration data. In each case, the model parameters (a, Q_{ss}^{0}, N_{ss}', etc.) were optimized to give the best fit to the data. The barrier resistance was assumed to be given by a power law of the surface resistivity so that $R = \mathcal{C}_0\rho/2a + A\rho^n$, where different values of A and n were considered for n and p-type substrates. The resulting optimized parameters are a probe radius of $a = 0.87\mu$m, an n-type contact resistance of $608\rho^{1.62}\Omega$ and a p-type contact resistance of $154\rho^{1.97}\Omega$ (ρ in units of Ω-cm). For the surface state model, a single value of Q_{ss}^{0} and N_{ss}' was used for both substrate types. The resulting optimized parameters are a probe radius of $a = 0.87\mu$m, an offset charge of $Q_{ss}^{0} = 5.8 \times 10^{-10}$C/cm^2, and a density of states of $N_{ss}' = 6.9 \times 10^{10}$eV^{-1}cm^{-2}. It is interesting to note that the interface state density seems lower than might be expected for an interface subjected to the seemingly crude beveling process, falling as it does between typical values for unannealed thermally grown oxides (low 10^{11}eV^{-1}cm^{-2}) and fully annealed Si-SiO$_2$ interfaces (low 10^{10}eV^{-1}cm^{-2}). From Figure 2, we can see that the barrier resistance model and the uniform state density model (which has two fewer parameters) both do an excellent job of accounting for the deviation of the calibration data from the ideal theory. However, as we will discuss in Section 5, the surface state model gives doping profiles which are closer to those expected from diffusion processes.

4 Effects of Probe Pressure and Penetration

When samples containing junctions are measured using spreading resistance, the peak resistance near the point on the bevel where the surface changes from n-type to p-type is much less than would be calculated for $p \cong n \cong n_i$. In addition, the peak gets lower and closer to the surface as the probe weight increases [22]. Two possible effects which might account for this behavior are finite probe penetration and the effect of probe pressure on the silicon properties.

It would seem that finite probe penetration would allow contact to underlying regions with higher carrier concentrations and lower resistivity. To model the effect of probe penetration, we assume that the probe contact actually is distributed within the sample with characteristic depth l_{pen}, so that the conductance measured is a weighted average of the conductance that would be measured as a function of depth. Assuming the effective contact area falls off exponentially with depth, the measured spreading resistance can be approximated by:

$$R_i = \frac{\sum_{j=i}^{m} \exp(-(x_j - x_i)/l_{\text{pen}})}{\sum_{j=i}^{m} \frac{\exp(-(x_j - x_i)/l_{\text{pen}})}{\hat{R}_{ij}}}, \tag{11}$$

where $\hat{R}_{ij}$ is the spreading resistance that would be measured if the probe contact was located at a depth x_j and the top surface at x_i. For a buried probe contact, the current can flow not only below but also above the probe, so we assume that the conductance due to a buried probe is a simple sum of the conductances due to the regions below and above the probe. Thus,

$$\hat{R}_{ij} = \frac{1}{2a\left(\sigma_j/\mathcal{C}_j + \sigma_{j-1}/\mathcal{C}_j^-\right)}, \tag{12}$$

where $\mathcal{C}_j$ is calculated in the usual way as described in Section 2, while $\mathcal{C}_j^-$ is calculated by considering the inverted set of layers seen by the probe looking upwards from $x = x_j$ with the air (above $x = x_i$) assumed to have zero conductance (see Fig. 1).

Using this model, we find that expected spreading resistance profiles are nearly independent of the probe penetration for values of penetration depth appropriate for well-conditioned probes. For example, Vandervorst and Maes [23] estimated probe penetration to be on the order of 10 nm, but it requires a penetration depth more than an order of magnitude larger than this for the peak resistance to drop into the range that is commonly measured. For large penetration depths (0.1-1.0μm), the peak resistance drops substantially, broadens and moves closer to the surface, all as observed for unconditioned probes or heavier probe weights [24].

The weak dependence of penetration on resistance measurements is a direct result of carrier spilling. Even though the simulated resistance may vary over orders of magnitude in 10 nm of effective depth along the bevel, at a given point on the bevel, the vertical carrier concentration varies much more slowly. The rapid variation in the on-bevel profile suggests that the finite size of the contact (as it samples a region along the bevel that increases with probe weight) is likely more important than the penetration in reducing and broadening the junction resistance peak.

The largest effect of pressure on the conductive properties of silicon, particularly for the on-bevel junction region, is a reduction in the bandgap [25], as the intrinsic carrier concentration varies as $n_i = \sqrt{N_C N_V} \exp(-E_g/2kT)$. Relative changes in the dielectric constant and carrier mobility (through effective mass and lifetime) are expected to be on the same order of magnitude as the bandgap reduction [25], but these factors enter only linearly rather than exponentially in determining conductivity. In extrinsic material, the band-gap reduction does not have a significant effect on the conductivity, so only relatively small changes due to pressure are expected (up to a factor of 2), although piezoresistive effects [26] may account for apparent differences in effective probe radius for differing substrate types and orientations.

Based on measurements of both the resistivity of intrinsic silicon as well as optical absorption, the reduction in silicon energy gap with pressure has been estimated to be 1-2×10^{-6}eV/bar [27, 28, 29], while the maximum pressure that the probes can exert is the yield strength of silicon, about 10^5bar [21, 30]. It is expected that the pressure exerted by probes is nearly independent of the probe weight as calculations show that probes which make good contact exceed the silicon yield strength and the resulting silicon deformation results in a larger contact area [21]. This pressure would result in a reduction in the band-gap of 0.1-0.2 eV. As shown in Figure 3, bandgap reductions on this order have a strong effect on the peak resistance near the on-bevel junction, but only minor effects on the rest of the profile. The resulting reduction in peak resistance for a bandgap reduction of 0.1-0.2 eV approaches typical measured values; however, there is a small shift in the peak towards the bulk, rather than towards the surface as observed experimentally [22].

In the calculations, the bandgap reduction was assumed to be uniform over the sampling depth of the probes. This assumption will overestimate the effect of band-gap narrowing, since the pressure will fall off with distance from the probe contact. However, as the name implies, spreading resistance is most sensitive to the conductivity near the contact, where the pressure is also the greatest. This is particularly true near an on-bevel junction since increasing the conductivity of the region immediately underneath the probe allows greater current flow to the underlying higher conductivity regions. In addition, acounting for the variation in bandgap reduction with depth would tend to shift the reistance peak towards the surface as the peak resistance would be measured when the minimum conductivity occurred at some depth below the contact, where it was less affected by bandgap narrowing.

5 Analysis System

In this section, we describe our analysis system, SERAPES (SprEading Resistance Analysis with Poisson Equation Solution) and give an example of its application. There four basic functions performed by the analysis system: calculation of resistance profiles from a doping profiles, calculation of doping profiles from resistance profiles, data smoothing and optimization of the contact/surface model parameters.

Calculation of the spreading resistance that would be measured for a given doping profile is at the heart of the system and is used in both doping-to-resistance and resistance-to-doping conversions, as well as the optimization of model parameters. SERAPES offers a choice of contact models, including the standard barrier resistance model (power law) with or without charge spilling and the surface state models described in Section 3. The analysis involves several steps. First, given a doping profile, the carrier concentrations are determined from Poisson's equation assuming Boltzmann statistics for the carrier concentrations and surface boundary conditions based on calculation of surface charge due to surface states. The resulting nonlinear second order boundary value problem is solved using finite difference discretization and Newton iteration. Because the presence of surface charges causes depletion or accumulation (particularly significant for lightly-doped substrates), additional grid points with spacing which increases with depth are added in the substrate to ensure accurate calculation of the substrate resistance. Next, the resistivity profile is calculated using the ASTM F723 standard [31], assuming total impurity ionization and neglecting compensation. Finally, the resistance is calculated using the EMAP algorithm of Berkowitz and Lux [10], with the barrier resistance as a function of surface potential added if appropriate.

Calculation of spreading resistance profiles from doping profiles simply requires a series of resistance calculations, with the top layer removed in between each step. This mode is particularly useful for characterizing the parameters of process models. As illustrated in Fig. 4, the simulated data can be used to generate simulated resistance data which can then be compared to measured resistance profiles. It is straightforward to include the spreading resistance analysis in a nonlinear optimization routine to find the best parameter set for a given set of experimental data. The process model can either be a simple analytic function, such as sums of Gaussians, or a process simulator (as in Fig. 4). We have used SERAPES extensively with SUPREM IV [32] to calculate process model parameters (such as dopant diffusivity) based on spreading resistance data [33, 34].

To calculate a doping profile directly from a resistance profile requires using the doping-to-resistance calculation within an optimization loop, as illustrated in Fig. 5. Typical calculation time for a junction profile with about 60 measured points is less than 10 s on a Silicon Graphics Indigo-2 R4000. The analysis begins by considering the deepest resistance value, assuming the substrate below that point is doped uniformly. Once the substrate doping is calculated, the profile is built up one layer at a time. At each step, an initial guess is made for the layer doping based on an extrapolation of the doping in previously calculated layers. The resistance is calculated and compared to the measured resistance. Based on the difference, improved guesses are made utilizing the numerical derivative of resistance with layer doping until the calculated and measured resistances match. Because there are as many layers as resistance values, it is possible to match the resistance profile exactly; however, the method is very subject to noise and smoothing of the resistance profile is usually necessary to get reasonable doping profiles. Because of carrier spilling, the method is particularly sensitive for retrograde profiles (doping increasing with depth) as the surface doping is overwhelmed by the spilling of carriers from the more heavily-doped underlying layers.

Since the calculation of doping from resistance is particularly sensitive to the derivative of resistance with depth, it is essential for the smoothed profile to minimize changes in the slope of the resistance profile. To this end, we utilize the cubic spline fitting algorithm with convexity constraints of Dierckx [35]. In this method, the resistance profile is divided by the user into regions where the curve is constrained to be either concave or convex, eliminating oscillations in the resistance profile which tend to become magnified upon converting to doping. This method has been found by Clarysse and Vandervorst [36] to give excellent results for spreading resistance analysis and we have found it to give results that are far superior to unconstrained smoothing techniques.

The final function performed by SERAPES is optimization of contact models parameters from calibration data. The technique used is similar to that used in calculating process model parameters, with the exception that in this case the doping profile is already known to be constant (with doping level calibrated from resistivity measurement) and instead, the surface parameters are varied to match the data. Given an initial guess for the model parameters, expected spreading resistance is calculated for each of the calibration samples. Based on the mean squared error between the measured and calculated resistance values, the parameters are optimized using a Levenberg-Marquardt algorithm (LMDIF) from MINPACK [37].

This work on spreading resistance analysis was originally motivated by our observation that doping profiles calculated using standard analysis techniques (no carrier spilling) were inconsistent with the predictions of process models, even for simple systems where constant diffusivities could be expected. In particular, in the tail region of profiles with low to moderate background doping ($< 10^{16}\mathrm{cm}^{-3}$), the calculated doping profiles dropped off precipitously compared to simulations. This behavior can be understood when carrier spilling is considered, since in the tail region, the carriers diffuse from the surface into the more lightly-doped bulk. This effect is particularly pronounced when the doping level is low (large Debye length) or when the doping gradient is large.

Figure 6 shows an example for a phosphorus profile following oxidation in steam at 900°C. The initial doping profile was measured using SRP and used as a starting profile for simulations using different dopant diffusivities. Without carrier spilling, it is not possible to find a diffusivity enhancement factor such that the simulated and calculated profiles match up. Adding carrier spilling through the solution of Poisson's equation greatly improves the agreement by extending the tail. Using a surface-state model rather that barrier resistance further improves the calculated profile, bringing it into agreement with the model predictions. It may be noted that none of the models do a good job of matching the concentration profile near the surface, as spreading resistance measurements consistently underestimate the doping concentration near the top surface due to bevel rounding and two-dimensional effects (missing material due to termination of bevel).

6 Conclusions

In summary, we have developed a spreading resistance analysis system (SERAPES) which includes carrier spilling through the solution of Poison's equation and is capable of calculating both expected resistance profiles from doping profiles as well as doping profiles from measured spreading resistance. The deviation of calibration data from ideal theory is accounted for by a choice of models including the standard barrier resistance model, as well as surface state models which provide a physical basis for a number of experimental observations. In addition, we include the reduction of energy gap with pressure, which can account for much of the discrepancy between simulated and measured values of the peak resistance near junctions.

7 Acknowledgements

This work was supported by SEMATECH/SRC Contract #90-MC-503. We would like to thank Harry Berkowitz for helpful discussions and information on the EMAP algorithm.

References

[1] J. Albers in *Emerging Semiconductor Technology*, ed. by D. C. Gupta and P. H. Langer, (American Society for Testing and Materials, 1986) p. 480.

[2] J. R. Ehrstein in *Emerging Semiconductor Technology*, ed. by D. C. Gupta and P. H. Langer, (American Society for Testing and Materials, 1986) p. 453.

[3] A. Casel and H. Jorke, Appl. Phys. Lett. **50**, 989 (1987).

[4] S. M. Hu, *J. Appl. Phys.* **53**, 1499 (1982).

[5] T. Clarysse, W. Vandervorst, and A. Casel, Appl. Phys. Lett. **57**, 2856 (1990).

[6] H. L. Berkowitz, *J. Electrochem. Soc.* **137**, 2581 (1990).

[7] H. L. Berkowitz, D. M. Burnell, R. J. Hilliard, R. G. Mazur and P. Rai-Choudhury, *Solid State Electron.* **33**, 773 (1990).

[8] P. A. Schumann and E. E. Gardner, *Solid State Electron.* **12**, 371 (1969).

[9] M. Pawlik in *Emerging Semiconductor Technology*, ed. by D. C. Gupta and P. H. Langer, (American Society for Testing and Materials, 1986) p. 502.

[10] H. L. Berkowitz and R. A. Lux, *J. Electrochem. Soc.* **128**, 1137 (1981).

[11] S. C. Choo, M. S. Leong, and K. L. Kuan, *Solid State Electron.* **19**, 561 (1976).

[12] S. C. Choo, M. S. Leong, C. B. T. Liem, and K. C. Kong, *Solid State Electron.* **33**, 783 (1990).

[13] M. S. Leong, S. C. Choo, Y. T. Lee, H. L. Ong and K. P. Ng, *J. Vac. Sci. Tech. B***10**, 426 (1992).

[14] A. M. Lin, D. A. Antoniadis and R. W. Dutton, *J. Electrochem. Soc.* **128**, 1131 (1981).

[15] S. T. Dunham and J. D. Plummer, *J. Appl. Phys.* **59**, 2551 (1986).

[16] W. Vandervorst and T. Clarysse, *J. Electrochem. Soc.* **137**, 679 (1990).

[17] R. G. Mazur and D. H. Dickey, *J. Electrochem. Soc.* **113**, 255 (1966).

[18] H. L. Berkowitz in **Semiconductor Fabrication: Technology and Metrology, ASTM STP 990**, ed. D. C. Gupta (American Society for Testing and Materials, Philadelphia, PA, 1988).

[19] R. Piessens, *J. Electrochem. Soc.* **130**, 468 (1983).

[20] T. Clarysse and W. Vandervorst, *Solid State Electron.* **33**, 1587 (1990).

[21] P. Kramer and L. J. Van Ruyven, *Solid State Electron.* **15**, 757 (1972).

[22] T. Clarysse and W. Vandervorst, *J. Vac. Sci. Tech. B***10**, 413 (1992).

[23] W. B. Vandervorst and H. E. Maes, *J. Appl. Phys.* **56**, 1583 (1984).

[24] R. G. Mazur and G. A. Gruber, *Solid State Tech.* , 64 (1981).

[25] W. Paul and D. M. Warschauer in **Solids Under Pressure**, W. Paul and D. M. Warschauer, eds. (McGraw-Hill Book Company, Inc., New York, NY, 1963) pp. 179-249.

[26] S. J. Fonash, in National Bureau of Standards Special Publication 400-10, Spreading Resistance Symposium Proceedings, J. Ehrstein, ed. (NBS, Gaithersburg, MD, 1974) p. 17.

[27] W. Paul and G. L. Pearson, *Phys. Rev.* **98**, 1755 (1955).

[28] W. Paul and D. M. Warshauer, *J. Phys. Chem. Solids* **5**, 102 (1958).

[29] T. E. Slykhouse and H. G. Drickamer, *J. Phys. Chem. Solids* **7**, 210 (1958).

[30] A. A. Giardini, *Am. Mineralogist*, **43**, 957 (1958).

[31] Annual Book of ASTM Standards (American Society for Testing and Materials, Philadelphia, PA, 1987).

[32] M. E. Law and R. W. Dutton, *IEEE Trans. CAD* **7**, 181 (1988).

[33] S. T. Dunham and N. Jeng, Appl. Phys. Lett. **59**, 2016 (1991).

[34] N. Jeng and S. T. Dunham, *J. Appl. Phys.* **72**, 2049 (1992).

[35] P. Dierekx, *Computing* **24**, 349 (1979).

[36] T. Clarysse and W. Vandervorst, *Solid State Electron.* **31**, 53 (1988).

[37] J. J. Moré in **Numerical Analysis, Lecture Notes in Mathematics 630**, ed. by G. A. Watson (Springer Verlag, 1977).

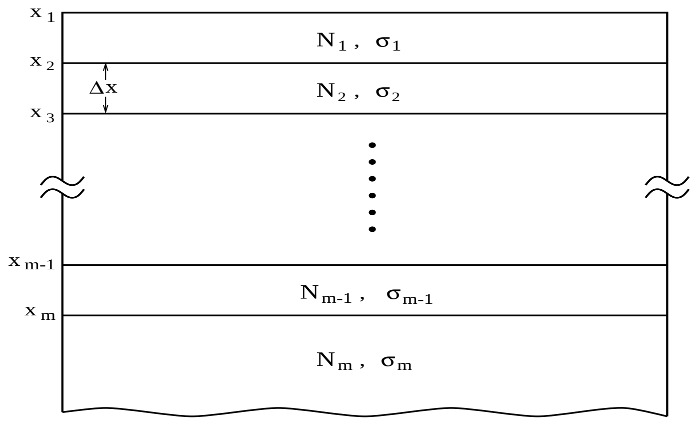

Figure 1: Sample structure considered for multilayer spreading resistance analysis.

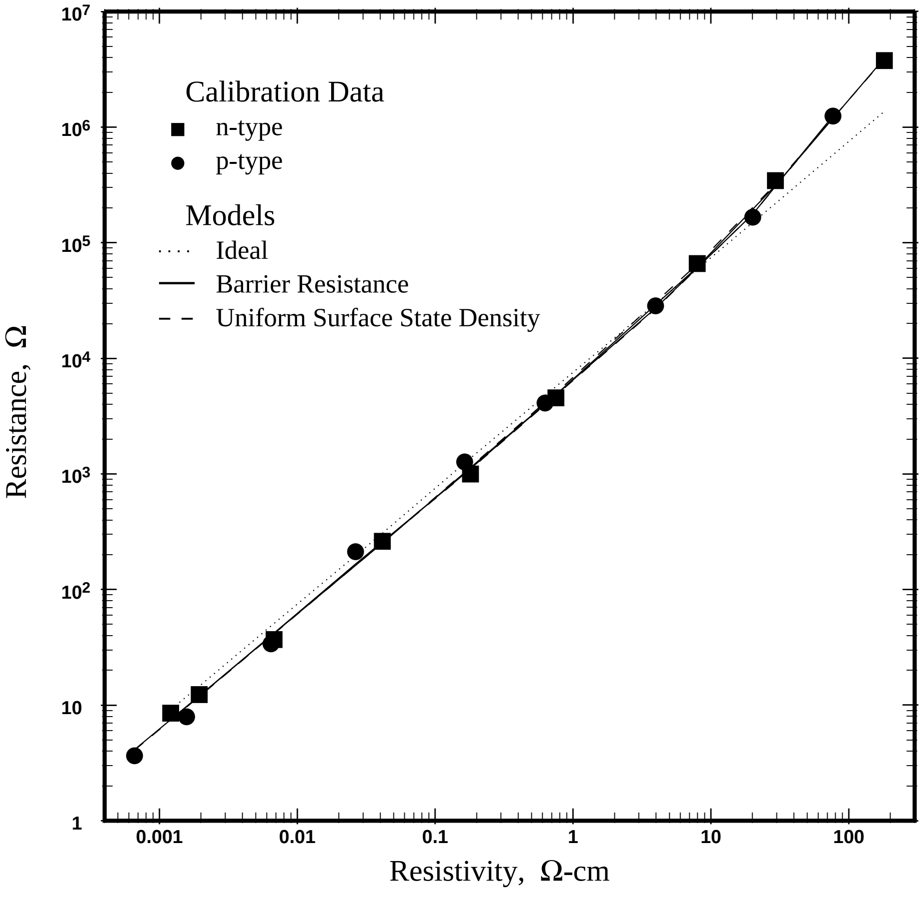

Figure 2: Comparison of models to calibration data. Separate curves are shown for n and p-type substrates, but the curves overlap for this set of calibration data.

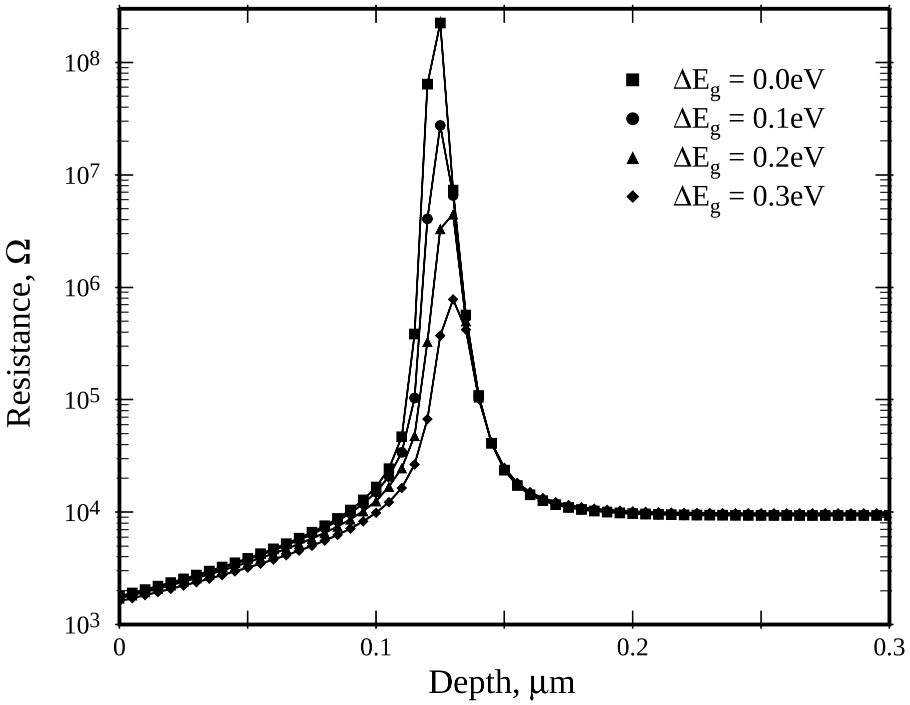

Figure 3: Effect of change in silicon energy gap due to probe pressure on calculated spreading resistance profile. Doping is a Gaussian n-type implant with peak of $4 \times 10^{18}\text{cm}^{-3}$ at the surface into a constant 10^{16}cm^{-3} p-type background. The metallurgical junction is at 0.2μm.

Figure 4: Block diagram for calculation of doping profiles from spreading resistance based on optimizing SUPREM IV parameters. SUPREM IV can be replaced by any process simulator or an analytic function.

Figure 5: Block diagram for calculation of doping profiles from spreading resistance data based on building up doping profile layer by layer from the substrate.

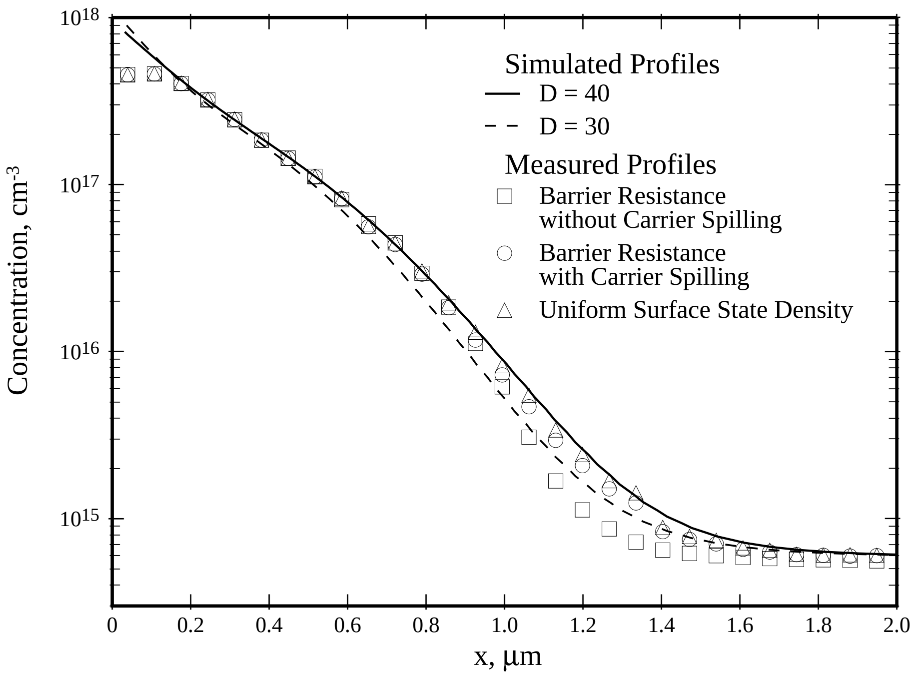

Figure 6: Doping profiles calculated from spreading resistance measurements using three different models and comparison to simulation predictions for two different values of dopant diffusivity. Probe effects such as bandgap narrowing were neglected.